

Towards muon-electron scattering at NNLO

Carlo M. Carloni Calame,^a Mauro Chiesa,^b Syed Mehedi Hasan,^a Guido Montagna,^{c,a}
Oreste Nicosini^a and Fulvio Piccinini^a

^a*INFN, Sezione di Pavia, Via A. Bassi 6, 27100 Pavia, Italy*

^b*LAPTh, CNRS, Annecy, F-74940*

^c*Dipartimento di Fisica, Università di Pavia, Via A. Bassi 6, 27100 Pavia, Italy*

E-mail: carlo.carloni.calame@pv.infn.it, mauro.chiesa@lapth.cnrs.fr,
syedmehe@pv.infn.it, guido.montagna@pv.infn.it,
oreste.nicosini@pv.infn.it, fulvio.piccinini@pv.infn.it

ABSTRACT: The recently proposed MUonE experiment at CERN aims at providing a novel determination of the leading order hadronic contribution to the muon anomalous magnetic moment through the study of elastic muon-electron scattering at relatively small momentum transfer. The anticipated accuracy of the order of 10ppm demands for high-precision predictions, including all the relevant radiative corrections. The theoretical formulation for the fixed-order NNLO photonic radiative corrections is described and the impact of the numerical results obtained with the corresponding Monte Carlo code is discussed for typical event selections of the MUonE experiment. In particular, the gauge-invariant subsets of corrections due to electron radiation as well as to muon radiation are treated exactly. The two-loop contribution due to diagrams where at least two virtual photons connect the electron and muon lines is approximated taking inspiration from the classical Yennie-Frautschi-Suura approach. The calculation and its Monte Carlo implementation pave the way towards the realization of a simulation code incorporating the full set of NNLO corrections matched to multiple photon radiation, that will be ultimately needed for data analysis.

KEYWORDS: Fixed target experiments, Precision QED, NNLO computations

Contents

1	Introduction	1
2	Electron (and muon) line radiation	3
3	YFS-inspired approximation of the full two-loop amplitude	6
4	Numerical results	8
4.1	Exact NNLO corrections from one leptonic line	11
4.2	Approximation to the full NNLO corrections	15
5	Summary and prospects	18

1 Introduction

The value of the anomalous magnetic moment of the muon, $a_\mu = (g-2)_\mu/2$, is a fundamental quantity in particle physics, that is presently known with a relative accuracy of 0.54ppm [1]. The muon anomaly, *i.e.* the deviation of the magnetic moment from the value predicted by Dirac theory, is due to quantum loop corrections stemming from the QED, weak and strong sector of the Standard Model (SM) [2, 3]. Hence, the comparison between theory and experiment provides a very stringent test of the SM and a deviation from the SM expectation is a monitor for the detection of possible New Physics signals.

There is a long-standing and puzzling muon $g - 2$ discrepancy between the measured value and the theoretical prediction, which presently exceeds the 3σ level. The current status of the SM theoretical prediction for the muon $g - 2$ has been very recently reviewed in Ref. [4].

Two new experiments, *i.e.* the presently running E989 experiment at Fermilab [5, 6] and the E34 experiment under development at J-PARC [7, 8], are expected to improve the current accuracy by a factor of four. This calls for a major effort on the theory side in order to reduce the uncertainty in the SM prediction, which is dominated by non-perturbative strong interaction effects as given by the leading order hadronic correction, a_μ^{HLO} , and the hadronic light-by-light contribution.

Traditionally, a_μ^{HLO} has been computed via a dispersion integral of the hadron production cross section in electron-positron annihilation at low energies [9–11]. Lattice QCD calculations are providing alternative evaluations of the leading order hadronic contribution [12–18]. Very recently the BMW collaboration has presented a precise determination of a_μ^{HLO} with an uncertainty of 0.7% [19], a central value larger than the ones obtained via dispersive approaches by about 2σ and in agreement with the BNL experimental determination [1]. New and promising algorithms are being developed for lattice QCD evaluation

of a_μ^{HLO} to reduce statistical fluctuations [20]. To clarify this situation, alternative and independent methods for the evaluation of a_μ^{HLO} are therefore more than welcome.

Following ideas first put forward in Refs. [21, 22] for the evaluation of a_μ as an integral over the photon vacuum-polarization function at negative q^2 , a novel approach has been recently proposed to derive a_μ^{HLO} from a measurement of the effective electromagnetic coupling constant in the space-like region via scattering data [23]. Shortly afterwards, the elastic scattering of high-energy muons on atomic electrons has been identified as an ideal process for such a measurement [24]¹ and a new experiment, MUonE, has been proposed at CERN to measure the differential cross section of μe scattering as a function of the space-like squared momentum transfer [27]. In order for this new determination of a_μ^{HLO} to be competitive with the traditional dispersive approach, the uncertainty in the measurement of the μe differential cross section must be of the order of 10ppm. This experimental target requires high-precision predictions for μe scattering, including all the relevant radiative corrections.

The extreme accuracy of MUonE demands for theoretical progress in the calculation of QED corrections to muon-electron scattering, resulting in next-generation Monte Carlo (MC) tools. For ultimate data analysis, the latter will have to include the full set of NNLO QED corrections combined with the leading (and, eventually, next-to-leading) logarithmic contributions due to multiple photon radiation. Quite recently, a number of steps have been already taken to achieve this goal. In Ref. [28], the full set of NLO QED and one-loop weak corrections was computed without any approximation and implemented in a fully exclusive MC generator. It is presently being used for simulation studies of MUonE events in the presence of QED radiation. Important results were also obtained at NNLO accuracy in QED. The master integrals for the two-loop planar and non-planar four-point Feynman diagrams were computed in Refs. [29, 30], by setting the electron mass to zero while retaining full dependence on the muon mass. A general procedure to extract leading electron mass terms for processes with large masses, such as muon-electron scattering, from the corresponding massless amplitude was given in Ref. [31] and supplemented with a subtraction scheme for QED calculations with massive fermions at NNLO accuracy [32]. The two-loop hadronic corrections to μe scattering were computed in Refs. [33, 34]. Also possible contamination from New Physics effects has been studied in Refs. [35, 36]. A comprehensive review of the current theoretical knowledge of the muon-electron scattering cross section for MUonE kinematical conditions has been published in Ref. [37].

In this paper, we present the calculation of the fixed-order NNLO QED photonic corrections and its implementation in a fully fledged MC generator (MESMER, Muon Electron Scattering with Multiple Electromagnetic Radiation²), which represents the first step towards the inclusion of the full set of NNLO corrections matched to multiple photon emission. In Section 2 the gauge invariant subset of photonic corrections on the single fermionic line (electron and muon) are discussed. These contributions are exact at NNLO accuracy, including all mass terms. The extension of the calculation to include the virtual amplitudes

¹A method to measure the running of the QED coupling in the space-like region using small-angle Bhabha scattering was proposed in Ref. [25] and applied to LEP data by the OPAL Collaboration [26].

²The MC code is not public yet, but we plan to make it available on a public repository soon.

involving the interference between the electron and muon line is discussed in Section 3. In this case the two-loop diagrams where at least two virtual photons connect the electron and muon lines are not completely known yet. However, thanks to the universality structure of the infrared (IR) contributions, the IR part of these NNLO virtual contributions can be taken into account by means of the classical Yennie-Frautschi-Suura (YFS) approach [38]. The real radiation matrix elements and phase space are exact, including all fermion mass terms. The described theoretical formulation is included in a fully exclusive NNLO MC code, needed for precision simulations at the MuonE experiment. The structure of the code is completely general and can be easily extended to include the nowadays missing exact NNLO contributions, thus removing the present source of approximation.

We performed several cross checks against the independent calculation of Ref. [39] for NNLO radiation stemming from the electron leg, finding perfect agreement. Thanks to this common effort, we agreed with the authors of Ref. [39] to proceed in parallel and make our results public at the same time.

By means of the developed MC code we illustrate in Section 4 numerical results relevant for typical running condition and event selections of the MUonE experiment. In particular, in Section 4.1 we show the impact of the exact NNLO photonic corrections due to electron and muon radiation on the main observables of interest for the MUonE experiment. In Section 4.2 we consider the impact of the approximate full NNLO photonic corrections on a subset of the same observables. In order to roughly estimate the uncertainty of the YFS approximation to the full NNLO amplitudes, a comparison of YFS at NLO is performed against the exact NLO calculation of Ref. [28]. A summary and future prospects are given in Section 5. The work presented in this paper represents the first fundamental step towards the implementation of a fully-fledged MC generator including the complete set of NNLO corrections matched to multiple photon emission.

2 Electron (and muon) line radiation

The complete set of NNLO QED corrections along the electron line entering the $\mu e \rightarrow \mu e$ process consists of three parts with contributions due to virtual and real photons. The virtual corrections give rise to ultraviolet divergencies that are computed in Dimensional Regularization (DR) and renormalized using the on-shell renormalization scheme. The three parts contributing to a given differential cross section at NNLO are the following ones:

- the $d\sigma_{\text{virt.}}^{\alpha^2}$ *two-loop* cross section, that consists of squared absolute value of diagrams 1a shown in Fig. 1 (summed with relative counterterms) and irreducible two-loop contributions due to diagrams as in 1b-1d in Fig. 1 in interference with the tree-level diagram;
- the $d\sigma_{1\gamma}^{\alpha^2}$ cross section, that corresponds to the *one-loop corrections to single photon* emission given by diagrams as in 2a-2b in Fig. 2;
- the $d\sigma_{2\gamma}^{\alpha^2}$ cross section associated to the *double bremsstrahlung* process $\mu e \rightarrow \mu e + \gamma\gamma$ given by contributions as in 2c-2d in Fig. 2.

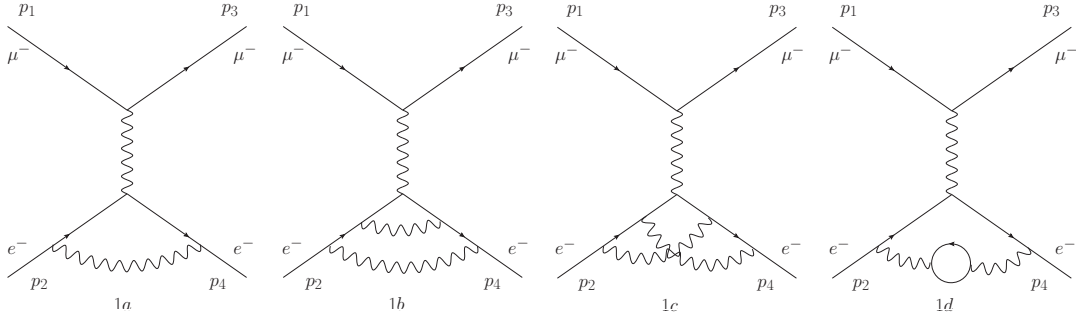


Figure 1. Virtual QED corrections to the electron line in $\mu e \rightarrow \mu e$ scattering. One-loop correction (diagram 1a); sample topologies for the two-loop corrections (diagrams 1b-1d). The blob in diagram 1d denotes an electron loop insertion. On-shell scheme counterterms are understood.

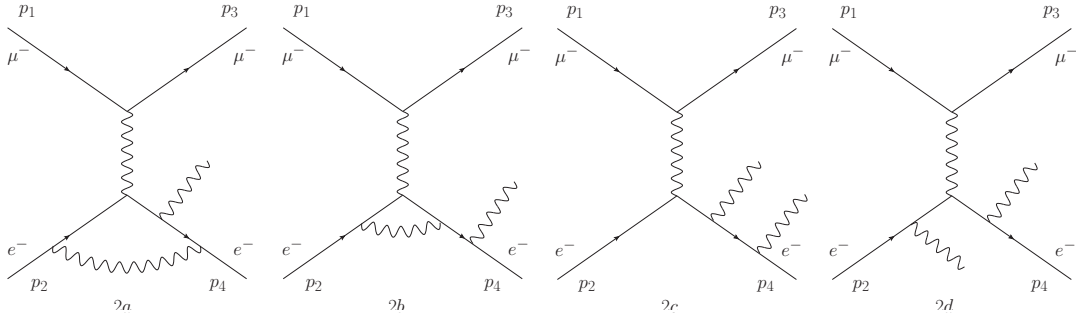


Figure 2. Sample diagrams for the one-loop QED corrections to single photon emission (diagrams 2a-2b); sample diagrams for the double bremsstrahlung process (diagrams 2c-2d).

All the above contributions are infrared-divergent quantities and we choose to regularize IR singularities by assigning a vanishingly small mass λ to the photon in the computation of virtual and real contributions. Then we introduce a soft-hard slicing separator ω_s , so that it acts as a fictitious energy resolution parameter of the photon radiation phase space, which is split into three sectors: the region labelled as $(0\gamma, \text{hard})$ corresponds to the region of unresolved radiation up to ω_s , the domain labelled as $(1\gamma, \text{hard})$ corresponds to the region with one resolved photon (with energy $> \omega_s$) and additional unresolved radiation up to ω_s , the domain $(2\gamma, \text{hard})$ corresponds to the region with two resolved photons, where both of them have energy larger than ω_s . According to the above described splitting, the pure $\mathcal{O}(\alpha^2)$ contribution to the cross section can be rewritten as follows:

$$d\sigma^{\alpha^2} = d\sigma_{0\gamma, \text{hard}}(\omega_s) + d\sigma_{1\gamma, \text{hard}}(\omega_s) + d\sigma_{2\gamma, \text{hard}}(\omega_s), \quad (2.1)$$

where

$$d\sigma_{0\gamma, \text{hard}}(\omega_s) = d\sigma_{0\gamma_s; 0\gamma_h}^{2\gamma \text{ virt}}(\lambda) + d\sigma_{1\gamma_s; 0\gamma_h}^{1\gamma \text{ virt}}(\lambda, \omega_s) + d\sigma_{2\gamma_s; 0\gamma_h}^{0\gamma \text{ virt}}(\lambda, \omega_s) \quad (2.2)$$

$$d\sigma_{1\gamma, \text{hard}}(\omega_s) = d\sigma_{0\gamma_s; 1\gamma_h}^{1\gamma \text{ virt}}(\lambda, \omega_s) + d\sigma_{1\gamma_s; 1\gamma_h}^{0\gamma \text{ virt}}(\lambda, \omega_s) \quad (2.3)$$

$$d\sigma_{2\gamma, \text{hard}}(\omega_s) = d\sigma_{0\gamma_s; 2\gamma_h}^{0\gamma \text{ virt}}(\omega_s) \quad (2.4)$$

and the subscripts and superscripts of Eqs. (2.2)-(2.4) indicate explicitly the number of virtual (virt), soft (s) and hard (h) photons. In Eq. (2.1), the cross section $d\sigma_{1\gamma,\text{hard}}(\omega_s)$ stands for the one-loop correction to the single bremsstrahlung with emission of a photon of energy greater than ω_s . Analogously, $d\sigma_{2\gamma,\text{hard}}(\omega_s)$ is the cross section corresponding to the radiation of two hard photons. The dependence on the photon mass parameter has been made explicit in Eqs. (2.2) and (2.3). Each term entering Eq. (2.1) is independent of λ . The radiation of real soft photons with energy smaller than ω_s is included by means of analytical eikonal factors [40–42]. The sum of the right-hand side of Eq. (2.1) is also independent of ω_s , so that Eq. (2.1) can be used to take into account any realistic experimental event selection.

The master formula with up to NNLO accuracy implemented in our MC generator reads as follows

$$d\sigma^{\text{NNLO}} = d\sigma^{\alpha^0} + d\sigma^{\alpha^1} + d\sigma^{\alpha^2}, \quad (2.5)$$

where $d\sigma^{\alpha^0}$ and $d\sigma^{\alpha^1}$ represent the tree-level and the NLO contributions, respectively. For definiteness and later use, we also define

$$d\sigma^{\text{LO}} = d\sigma^{\alpha^0}, \quad (2.6)$$

$$d\sigma^{\text{NLO}} = d\sigma^{\alpha^0} + d\sigma^{\alpha^1}. \quad (2.7)$$

For the calculation of the radiative corrections with one virtual photon and the double bremsstrahlung process, all the Feynman diagrams were manipulated with the help of the algebraic manipulation program FORM [43, 44], keeping full dependence on the lepton masses. The evaluation of one-loop tensor coefficients and scalar functions is performed using the package COLLIER [45]³. As a cross-check, we compared our QED calculation of the one-loop Dirac and Pauli form factors with the Abelian limit of the QCD results given in Ref. [48] (see also [49]), converting the soft-IR pole in DR to the logarithm involving the photon mass λ according to the rule $(4\pi\mu^2)^\epsilon \Gamma(1+\epsilon)/\epsilon \rightarrow \ln \lambda^2$ [42], finding perfect agreement. For the virtual two-loop corrections, we resorted to the calculation of the $\mathcal{O}(\alpha^2)$ QED form factors of Ref. [50], where IR divergences are parameterized in terms of the fictitious photon mass λ and all finite lepton mass effects are kept⁴. In the latter, the result is expressed in terms of Harmonic Polylogarithms and we checked that the asymptotic expansion for large momentum transfer agrees with the high-energy limit of the two-loop form factors given in Refs. [51, 52], up to constant terms. It is worth mentioning that the QCD NNLO form factors have been calculated also in Ref. [53], with partial results relevant for the full three-loop form factor calculation in Refs. [54–57].

The $\mathcal{O}(\alpha^2)$ QED form factors also contain the contribution of the diagram with a vacuum polarization insertion on the vertex photonic correction (see Figure 1, diagram 1d), due to the same lepton of the external legs. This contribution is enhanced by a term proportional to $\alpha^2 L^3$, where $L = \ln\left(\frac{-t}{m^2}\right)$ represents the collinear logarithm, which is, in any

³Several cross-checks have been performed with the package LOOPTOOLS [46, 47] finding very good agreement.

⁴We thank P. Mastrolia and A. Primo for providing us with updated exact expressions of the form factors.

case, exactly cancelled by the emission of a real leptonic pair, when the latter is integrated on the available phase space [58]. For this reason we define our NNLO photonic corrections by removing the contribution due to the fermionic loop, which will be investigated in the future with real leptonic pair emission. This $N_f = 1$ contribution to the Dirac and Pauli form factors has been computed independently in DR and found to agree with Eqs. (94) and (95) of Ref. [59]. The final result is finite and independent of the regularization scheme adopted in the intermediate steps.

3 YFS-inspired approximation of the full two-loop amplitude

In this section, we discuss how the full two-loop virtual QED corrections can be approximated to catch its complete IR structure. The aim is to implement a full, although approximate, two-loop QED correction to the process $\mu e \rightarrow \mu e$ which includes correctly at least all the IR parts. In particular, we are approximating only the diagrams obtained by inserting a virtual photon into a QED one-loop box diagram, all the rest of the corrections being exact. We remark that also the full one-loop corrections to the radiative processes $\mu^\pm e^- \rightarrow \mu^\pm e^- \gamma$ are needed and calculated exactly, including box and pentagon diagrams. The latter are calculated with the techniques described above for one-loop corrections⁵.

The full two-loop virtual amplitude is built-up exploiting the YFS analysis of IR divergencies in QED [38]. The starting point are Eqs. (2.2a-c) of the original YFS paper, where the exact n -loop amplitude is formally written extracting order by order IR factors in an iterative way. Stopping at two-loop, their equations can be written as

$$\begin{aligned}
\mathcal{M}^{\alpha^0} &= \mathcal{T} \\
\mathcal{M}^{\alpha^1} &= Y\mathcal{T} + \mathcal{M}^{\alpha^1,\text{R}} \\
\mathcal{M}^{\alpha^2} &= \frac{1}{2}Y^2\mathcal{T} + Y\mathcal{M}^{\alpha^1,\text{R}} + \mathcal{M}^{\alpha^2,\text{R}} \\
&= -\frac{1}{2}Y^2\mathcal{T} + Y\mathcal{M}^{\alpha^1} + \mathcal{M}^{\alpha^2,\text{R}}
\end{aligned} \tag{3.1}$$

where \mathcal{T} represents the tree level amplitude, \mathcal{M}^{α^n} are the exact n -loop amplitudes, Y (of order α) is the YFS IR virtual factor and the superscript R indicates the non-IR remnant of the amplitude. We stress that IR divergencies are confined only in the terms containing at least one Y factor.

Restricting to the process under consideration and using momenta labelling as in Fig. 1, the IR factor Y explicitly reads (see also Refs. [61–64])

$$Y = \sum_{i,j=1,4}^{j \geq i} Y_{ij} = Y_e + Y_\mu + Y_{e\mu} \tag{3.2}$$

⁵For the full one-loop QED corrections to the process of single-photon emission, we find agreement with the matrix elements calculated by using the RECOLA-COLLIER package [45, 60]. Particular attention is being paid in order to make the pentagon amplitudes numerically stable in phase-space regions where the external photon momentum tends to be soft. The details are beyond the scope of the present paper and will be possibly discussed elsewhere.

where

$$Y_{ij} = \begin{cases} \frac{1}{8} \frac{\alpha}{\pi} Q_i^2 [B_0(0, m_i^2, m_i^2) - 4m_i^2 C_0(m_i^2, 0, m_i^2, \lambda^2, m_i^2, m_i^2)] & \text{for } i = j \\ \frac{\alpha}{\pi} Q_i Q_j \vartheta_i \vartheta_j \left[p_i \cdot p_j C_0(m_i^2, (\vartheta_i p_i + \vartheta_j p_j)^2, m_j^2, \lambda^2, m_i^2, m_j^2) + \right. \\ \left. + \frac{1}{4} B_0((\vartheta_i p_i + \vartheta_j p_j)^2, m_i^2, m_j^2) \right] & \text{for } i \neq j \end{cases} \quad (3.3)$$

$$\begin{aligned} Y_e &= Y_{24} + Y_{22} + Y_{44} \\ Y_\mu &= Y_{13} + Y_{11} + Y_{33} \\ Y_{e\mu} &= Y_{12} + Y_{14} + Y_{23} + Y_{34} \end{aligned} \quad (3.4)$$

In Eq. (3.3), Q_i is the charge of particle i in positron charge units, $\vartheta_i = -1$ (1) for an incoming (outgoing) fermion and the arguments of the scalar one-loop functions B_0 and C_0 follow COLLIER/LOOPTOOLS conventions. We stress that Y_a with $a = e, \mu, e\mu$ are the factors which factorize the IR divergence of the diagrams obtained by dressing the underlying amplitude with an extra virtual photon attached to the electron ($a = e$) or muon ($a = \mu$) line or connecting them ($a = e\mu$). An analogous separation holds for the exact one-loop amplitude \mathcal{M}^{α^1} and its non-IR remnant $\mathcal{M}^{\alpha^1, \text{R}}$ of Eq. (3.1), *i.e.* we can write $\mathcal{M}^{\alpha^1, \text{R}} = \mathcal{M}_e^{\alpha^1, \text{R}} + \mathcal{M}_\mu^{\alpha^1, \text{R}} + \mathcal{M}_{e\mu}^{\alpha^1, \text{R}}$.

We can now approximate the complete two-loop virtual amplitude \mathcal{M}^{α^2} by writing

$$\begin{aligned} \mathcal{M}^{\alpha^2} &\simeq \widetilde{\mathcal{M}}^{\alpha^2} = \mathcal{M}_e^{\alpha^2} + \mathcal{M}_\mu^{\alpha^2} + \mathcal{M}_{e\mu, 1\text{L} \times 1\text{L}}^{\alpha^2} \\ &\quad + \frac{1}{2} Y^2 \mathcal{T} + Y \mathcal{M}^{\alpha^1, \text{R}} \\ &\quad - \left(\frac{1}{2} Y_e^2 \mathcal{T} + Y_e \mathcal{M}_e^{\alpha^1, \text{R}} \right) - \left(\frac{1}{2} Y_\mu^2 \mathcal{T} + Y_\mu \mathcal{M}_\mu^{\alpha^1, \text{R}} \right) \\ &\quad - \left(Y_e Y_\mu \mathcal{T} + Y_e \mathcal{M}_\mu^{\alpha^1, \text{R}} + Y_\mu \mathcal{M}_e^{\alpha^1, \text{R}} \right), \end{aligned} \quad (3.5)$$

where in the second line of Eq. (3.5) we have put $\mathcal{M}^{\alpha^2, \text{R}} = 0$. With little algebra, the previous definition can be also recast in the following form

$$\begin{aligned} \widetilde{\mathcal{M}}^{\alpha^2} &= \mathcal{M}_e^{\alpha^2} + \mathcal{M}_\mu^{\alpha^2} + \mathcal{M}_{e\mu, 1\text{L} \times 1\text{L}}^{\alpha^2} \\ &\quad + \frac{1}{2} Y_{e\mu}^2 \mathcal{T} + Y_{e\mu} (Y_e + Y_\mu) \mathcal{T} + (Y_e + Y_\mu) \mathcal{M}_{e\mu}^{\alpha^1, \text{R}} + Y_{e\mu} \mathcal{M}^{\alpha^1, \text{R}}. \end{aligned} \quad (3.6)$$

In Eq. (3.5), in the first row, $\mathcal{M}_e^{\alpha^2}$ ($\mathcal{M}_\mu^{\alpha^2}$) represents the set of two-loop diagrams where the two virtual photons are both attached to the electron (muon) line, whereas $\mathcal{M}_{e\mu, 1\text{L} \times 1\text{L}}^{\alpha^2}$ represents the diagrams where one photon is on the electron line and the other one on the muon line⁶. The second row contains the full IR part of Eq. (3.1). The third and fourth rows finally subtract from the second one the IR content already accounted for in $\mathcal{M}_e^{\alpha^2} + \mathcal{M}_\mu^{\alpha^2} + \mathcal{M}_{e\mu, 1\text{L} \times 1\text{L}}^{\alpha^2}$. In other words, the approximation $\widetilde{\mathcal{M}}^{\alpha^2}$ misses only the non-IR remnant of the two-loop diagrams where at least two photons connect the electron and

⁶This set can be easily computed exactly, for instance by using one-loop renormalized vertex form factors.

muon lines, which are not known yet for the process under consideration. This is made possibly more explicit in the equivalent form of Eq. (3.6), where each term in the second row, approximately accounting for the missing contributions, has a factor with an “ $e\mu$ ” subscript. Despite being incomplete, the exact IR structure of the full two-loop amplitude, with massive electron and muon, is present in Eqs. (3.5) and (3.6): on the one side this can be used to cross-check the IR part of the final calculation once it is available, on the other side it can be implemented into the Monte Carlo generator for phenomenological studies. We stress that, when we add $2\mathcal{R}(\widetilde{\mathcal{M}}^{\alpha^2}\mathcal{T}^*)$ to the rest of the exact $\mathcal{O}(\alpha^2)$ contributions, the sum is perfectly independent of the fictitious photon mass λ and thus the result is meaningful.

On the accuracy side, heuristic considerations, also based upon an analogous numerical analysis at one-loop order, bring us to estimate the size of the dominant missing non-IR $\mathcal{O}(\alpha^2)$ corrections to be in the range of a few $(\frac{\alpha}{\pi})^2 \ln^2(m_\mu^2/m_e^2) \simeq 6 \times 10^{-4}$, as discussed later.

4 Numerical results

In this Section, we show and discuss the phenomenological results obtained by using a fully differential MC code, MESMER, which implements the theoretical approach described in Section 2 and Section 3. We adopt the parameters and typical running condition of the MUonE experiment already described in detail in Ref. [28], which we briefly remind here: the reference frame is the laboratory frame, where the energy of the incoming μ^\pm is $E_\mu^{\text{beam}} = 150$ GeV, the electron is assumed to be at rest inside a bulk target and thus $\sqrt{s} \simeq 0.405541$ GeV. In this kinematical condition, the collinear logarithms $L_e = \ln(s/m_e^2)$ and $L_\mu = \ln(s/m_\mu^2)$ are of the order of $L_e \simeq 13.4$ and $L_\mu \simeq 2.7$, respectively. We study the numerical impact of QED NNLO photonic corrections to observables assuming the following event selections (Setup 2 and Setup 4 of Ref. [28]):

1. $\vartheta_e, \vartheta_\mu < 100$ mrad and $E_e > 1$ GeV (i.e. $t_{ee} \lesssim -1.02 \cdot 10^{-3}$ GeV²). The angular cuts model the typical acceptance conditions of the experiment and the electron energy threshold is imposed to guarantee the presence of two charged tracks in the detector (Setup 1);
2. the same criteria as above, with the additional acoplanarity cut $|\pi - |\phi_e - \phi_\mu|| \leq 3.5$ mrad. We remind the reader that this event selection is considered in order to mimic an experimental cut which allows to stay close to the elasticity curve given by the tree-level relation between the electron and muon scattering angles (Setup 2)⁷,

where $t_{ee} = (p_2 - p_4)^2$, $(\vartheta_e, \phi_e, E_e)$ and $(\vartheta_\mu, \phi_\mu, E_\mu)$ are the scattering and azimuthal angles and the energy, in the laboratory frame, of the outgoing electron and muon, respectively.

⁷The acoplanarity cut partially removes radiative events and thus enhances the fraction of quasi-elastic events, as illustrated by Fig. 3 of Ref. [28]. Here it is used merely as a possible cut for selecting elastic events, without pretending it to be realistic. Indeed, from the experimental point of view, the extraction of the hadronic contribution to the running of $\alpha(t)$ could benefit from selecting events in the elastic region.

For Setup 1 and Setup 3 of Ref. [28], with $E_\gamma > 0.2$ GeV, the NNLO QED photonic effects are similar in size to the ones presented here and therefore are not considered for the sake of brevity.

The input parameters for the simulations are set to

$$\alpha = 1/137.03599907430637 \quad m_e = 0.510998928 \text{ MeV} \quad m_\mu = 105.6583715 \text{ MeV}$$

and the considered differential observables are the following ones:

$$\frac{d\sigma}{dt_{ee}}, \quad \frac{d\sigma}{dt_{\mu\mu}}, \quad \frac{d\sigma}{d\vartheta_e}, \quad \frac{d\sigma}{d\vartheta_\mu}, \quad \frac{d\sigma}{dE_e}, \quad \frac{d\sigma}{dE_\mu}, \quad (4.1)$$

where $t_{\mu\mu} = (p_1 - p_3)^2$.

For definiteness, we remark that all calculations and simulations are performed in the center of mass (c.m.) frame and then the momenta are boosted to the laboratory frame, where the initial-state electron is at rest. The soft-hard separator ω_s , not Lorentz invariant, is defined in the c.m. reference frame and its default value is taken to be $\omega_s = 10^{-5} \times \sqrt{s}/2$. We checked both at integrated and differential level that the cross-sections are independent of the unphysical parameters λ and ω_s .

Within the full set of NLO and NNLO QED corrections, there are three gauge-invariant subsets of photonic contributions corresponding to:

1. virtual and real corrections along the electron line;
2. virtual and real corrections along the muon line;
3. the rest of the virtual and real corrections, including box-like contributions, up-down interference of real photon radiation and so on.

In Section 4.1 we present the exact QED NNLO photonic corrections for the distributions of Eq. (4.1) for the electron and muon line separately. In Section 4.2 we present the results for our approximation to the full QED NNLO virtual photonic corrections described in Sect. 3⁸. All the figures show the difference in per cent between the NNLO and NLO predictions relative to the tree-level differential cross section, *i.e.*

$$\Delta_{\text{NNLO}}^i = 100 \times \frac{d\sigma_{\text{NNLO}}^i - d\sigma_{\text{NLO}}^i}{d\sigma_{\text{LO}}}, \quad (4.2)$$

where $i = e, \mu, f$ stand for electron-line only, muon-line only and the full set of NNLO corrections. For the sake of clarity, all the figures contain insets which display the NLO corrections w.r.t. the LO predictions, according to

$$\Delta_{\text{NLO}}^i = 100 \times \frac{d\sigma_{\text{NLO}}^i - d\sigma_{\text{LO}}}{d\sigma_{\text{LO}}}. \quad (4.3)$$

In order to quantify the purely photonic effects, we do not include any vacuum polarization correction neither in the NLO nor in the NNLO cross sections. The absolute values and shapes of the observables can be obtained from Ref. [28]. In this Section, figures with two

σ (μb)	Setup 1		Setup 2	
	$\mu^-e^- \rightarrow \mu^-e^-$	$\mu^+e^- \rightarrow \mu^+e^-$	$\mu^-e^- \rightarrow \mu^-e^-$	$\mu^+e^- \rightarrow \mu^+e^-$
σ_{LO}	245.038910(1)			
σ_{NLO}^e	255.5500(7)		223.4387(6)	
σ_{NLO}^μ	244.9707(1)		244.4136(1)	
σ_{NLO}^f	255.1176(5)	255.8437(5)	222.8545(3)	222.7714(3)
σ_{NNLO}^e	255.5725(5)		224.4796(4)	
σ_{NNLO}^μ	244.9706(1)		244.4154(1)	
σ_{NNLO}^f	<i>255.205(1)</i>	<i>256.092(1)</i>	<i>224.041(1)</i>	<i>224.088(1)</i>

Table 1. Cross sections (in μb) and relative corrections for the processes $\mu^-e^- \rightarrow \mu^-e^-$ and $\mu^+e^- \rightarrow \mu^+e^-$, in the two different setups described in the text. The symbols $\sigma_{(\text{N})(\text{N})\text{LO}}^{e/\mu/f}$ stand for the cross sections with corrections along the electron line only, along the muon line only and the full approximate contributions, respectively, with the perturbative accuracy given by the subscripts. The digits in parenthesis correspond to 1σ MC error. Italicized numbers in the last row indicate that in this cross-section the full two-loop amplitude is approximated as described in Section 3.

panels show corrections in Setup 1 on the left and in Setup 2 on the right, unless stated otherwise.

Before showing the effects on the distributions, we quote in Tab. 1 the integrated cross-sections for the two Setups, showing the different classes of corrections. The symbols $\sigma_{(\text{N})(\text{N})\text{LO}}^{e/\mu/f}$ stand for the cross sections with corrections along the electron line only, along the muon line only and the full approximate contributions, respectively, with the perturbative accuracy given by the subscripts. The subsets of corrections coming from electron or muon line separately are the same for both processes $\mu^-e^- \rightarrow \mu^-e^-$ and $\mu^+e^- \rightarrow \mu^+e^-$, as expected. For Setup 1 the correction to the cross section along the electron line amounts to less than 0.01% with positive sign, with respect to the NLO prediction, while the correction along the muon line is below the 10^{-5} level, still compatible with zero within the statistical integration uncertainty. For Setup 2 the correction along the electron line becomes of the order of +0.45% and the one along the muon line below the 0.01% level. The numbers in the last row of the table are italicized to indicate that these cross-sections are approximate according to the discussion of Sect. 3. Numerically, the full corrections in Setup 1 amount to about +0.04%, with respect to the NLO prediction, for the process with μ^- beam, while it amounts to about +0.1% with μ^+ in the initial state. Given the inherent uncertainty, roughly estimated to be of the order of 0.06% in Section 3, these estimates can not be considered conclusive yet. When including the acoplanarity cut (Setup 2), the approximate NNLO corrections become of the order of 0.5%, because of IR effects enhancement, thus being more robust in view of the intrinsic uncertainty of the approximate prediction discussed before.

⁸We remind the reader that in our approximation any real radiation contribution is exact, including all finite mass effects.

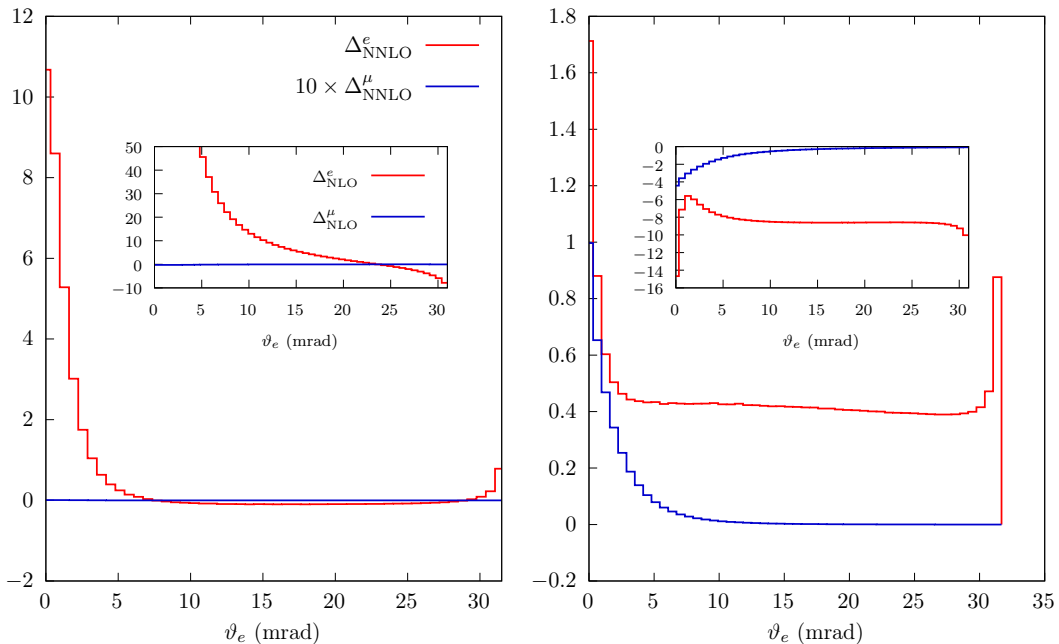


Figure 3. Red histograms: NNLO corrections, according to Eq. (4.2), along the electron line, for the $\mu^\pm e^- \rightarrow \mu^\pm e^-$ processes, as a function of the electron scattering angle in the laboratory frame, ϑ_e ; blue histogram: $10 \times \text{NNLO}$ corrections along the muon line. Left panel: differential distribution in the presence of acceptance cuts only (Setup 1); right panel: the same as in the left panel with the additional acoplanarity cut of Setup 2. The insets report the NLO corrections, according to Eq. (4.3); the blue line represents directly Eq. (4.3) without any multiplicative factor.

4.1 Exact NNLO corrections from one leptonic line

In this Section we present the results for the relative contribution of the NNLO photonic corrections to the differential distributions according to Eq. (4.2). In particular, we consider the exact NNLO corrections due to electron and muon radiation, which represent different gauge invariant subsets of the whole NNLO corrections. The correction along the electron line is particularly important, because, as shown in Ref. [28], already at NLO level it is enhanced w.r.t. the radiation from the muon line, as a consequence of the small ratio m_e/m_μ . Moreover, it gives the bulk of the correction for some observables or in particular phase-space regions.

Figure 3 shows the effects of NNLO corrections, according to Eq. (4.2), for the observable $d\sigma/d\vartheta_e$. In Setup 1, the correction along the electron line (red histogram) is flat over a large portion of scattering angles larger than about 5 mrad, being of the order of a few 0.1% at most, and displays a step increase for $\vartheta_e \rightarrow 0$, where it reaches the order of 10%. As can be seen from the inset, the electron scattering angle distribution $d\sigma/d\vartheta_e$ is quite sensitive to NLO corrections, in particular for small values of ϑ_e , where the NLO correction becomes particularly enhanced as due to hard bremsstrahlung effects and because the tree-level differential cross section tends to zero. As a consequence, the increase of the NNLO correction for $\vartheta_e \rightarrow 0$ is not surprising. Contrarily to the correction along the electron line, the one

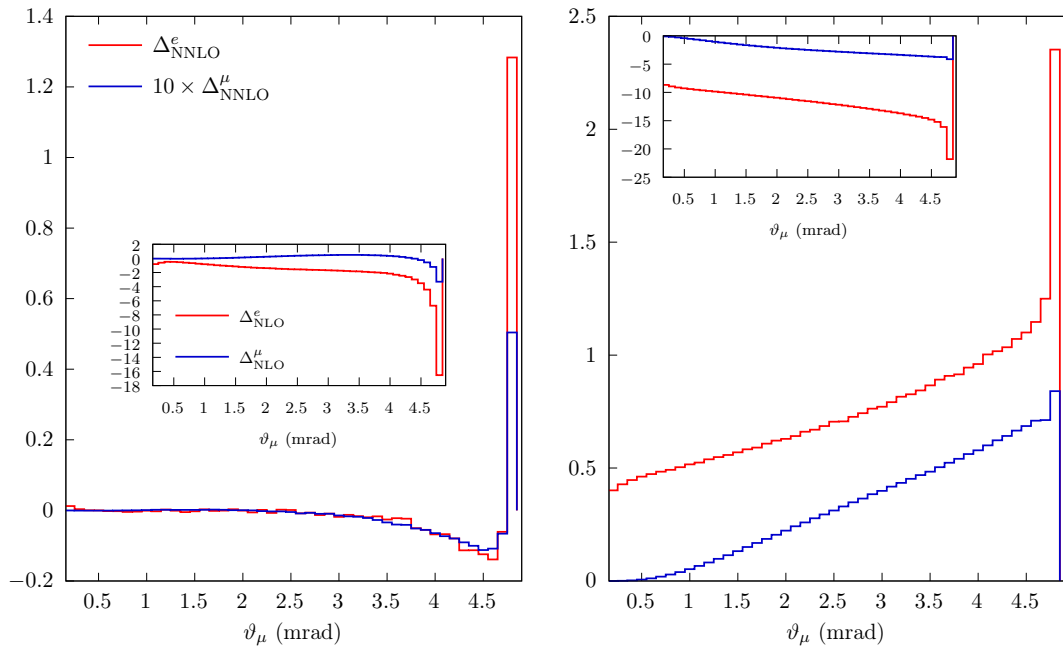


Figure 4. The same as Fig. 3 for the muon scattering angle ϑ_μ .

along the muon line (blue histogram, multiplied by a factor of 10) is flat over the whole ϑ_e angular spectrum and invisible on the plot scale. The shape of the corrections remains qualitatively the same also in the presence of the additional acoplanarity cut of Setup 2, even if the size of the correction along the electron line becomes larger ($\sim +0.4\%$) for a wide range of ϑ_e . This is a consequence of the effects of the IR enhancement introduced effectively by the acoplanarity cut. Indeed the NLO correction grows to negative values of the order of -8% . In Setup 2, the NNLO correction due to electron radiation is about $+1.7\%$ for $\vartheta_e \rightarrow 0$ mrad and amounts to 0.8% at the opposite kinematical boundary. Even in the presence of the acoplanarity cut, the NNLO correction along the muon line remains flat over the entire spectrum, increasing to about $+0.1\%$ for $\vartheta_e \rightarrow 0$, consistently with the behaviour of the NLO correction shown in the inset.

Figure 4 shows the effects of NNLO corrections for the observable $d\sigma/d\vartheta_\mu$ ⁹. In Setup 1 (left panel), the NNLO correction along the electron line (red histogram) has a non-trivial shape, remaining of the order of 0.01% and dropping to about -0.14% from 2.5 mrad to 4.5 mrad, with a sharp increase in the last two bins, reaching the level of $+1.3\%$ at the kinematical limit. Interestingly, the NNLO correction along the muon line (blue histogram) displays the same shape of the correction along the electron line but with a reduction in size by a factor of ten (a factor of 30 in the last bin). The shapes of the corrections change

⁹In this case, we do not show muon scattering angles $\vartheta_\mu < 0.16$ mrad because the corrections are huge and would spoil the readability of the plots. The reason for this feature is that the LO prediction becomes negligible in the above angular range, as a consequence of the applied acceptance cuts, while the single- and double-radiative events populate the region.

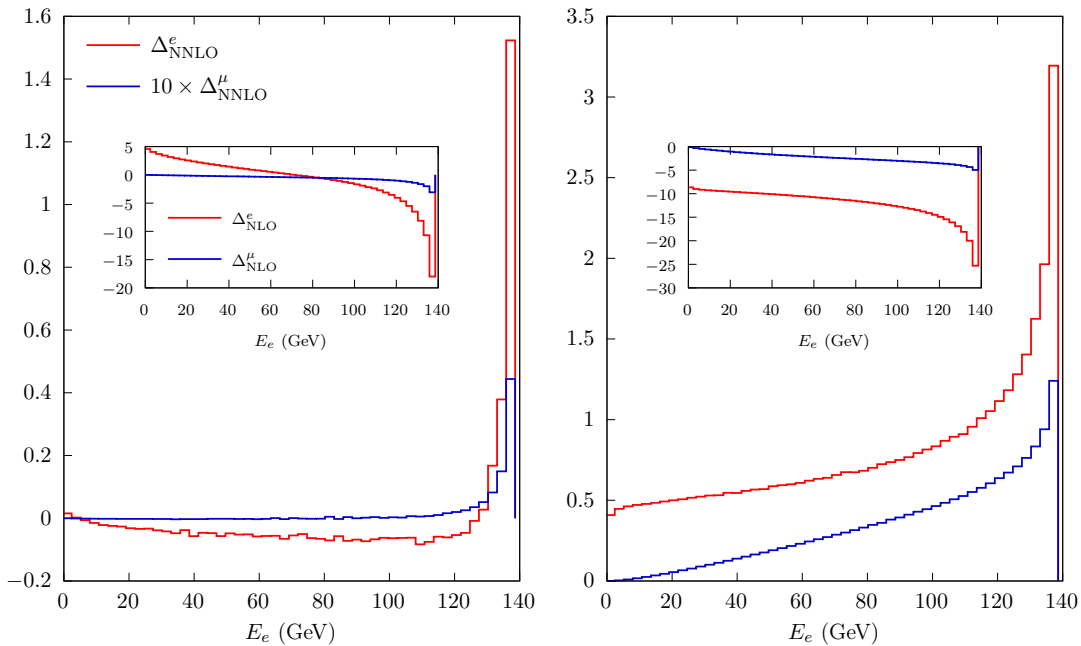


Figure 5. The same as Fig. 3 for the electron energy E_e .

when the acoplanarity cut is added (right panel). In this case the correction along the electron line (red histogram) becomes an increasing function of ϑ_μ , ranging from +0.4% for ϑ_μ in the left corner of the plot to about 2.4% at the upper kinematical limit. This large and positive correction can be understood by looking at the inset, which shows that the NLO correction varies monotonically between -8% and -22% , as enhanced by IR effects introduced by the acoplanarity cut. The NNLO correction along the muon line displays qualitatively a similar shape and reaches about $+0.08\%$ at the upper kinematical limit.

Figure 5 shows the effects of NNLO corrections for the observable $d\sigma/dE_e$. In Setup 1, the NNLO correction along the electron line is negative, not exceeding the -0.1% level up to energies of the order of 120 GeV, where it shows a change of slope towards positive values, reaching the level of $+1.5\%$ for the maximum available energy. This feature reflects the behaviour of the NLO correction, shown in the inset, which ranges from $+5\%$ to -5% in the region $m_e < E_e < 120$ GeV and drops to about -18% at the kinematical limit, signalling the presence of enhanced IR effects because of missing available phase space for real photon emission. For Setup 2, the IR enhancement of the NNLO corrections is visible over the entire energy range, changing monotonically from about $+0.5\%$ for $E_e \rightarrow m_e$ to about 3.2% at the upper kinematical limit. The NNLO correction along the muon line is similar in shape to the one along the electron line but with reduced size by about a factor of 30.

In Fig. 6 we show the effects of NNLO corrections on $d\sigma/dE_\mu$. In the case of Setup 1, the shapes of the contributions along the electron line (red histogram) and the muon line (blue histogram) are quite different. The former displays a sharp peak, of the order of $+0.18\%$

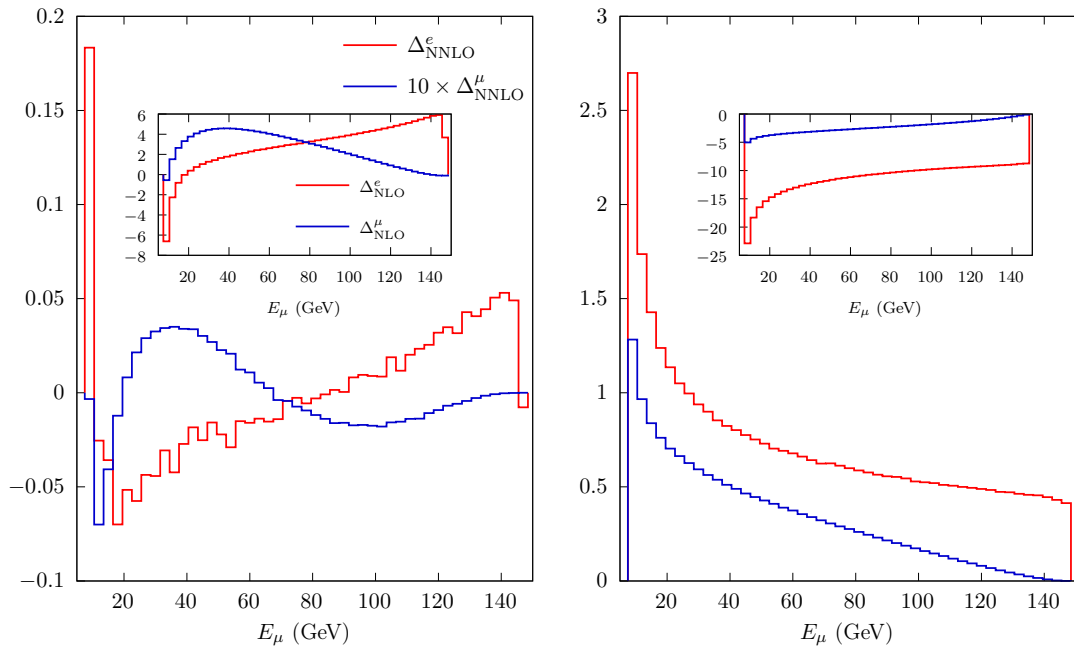


Figure 6. The same as Fig. 3 for the muon energy E_μ .

in the first bin for the minimum muon energy and then ranges monotonically from -0.07% up to about $+0.05\%$. The correction along the muon line shows a more rich structure, never exceeding the size of 0.006% . When including the acoplanarity cut (Setup 2), the NNLO correction along the electron line becomes a monotonically decreasing function of E_μ , ranging from $+2.7\%$ to about $+0.4\%$. The NNLO correction along the muon line (in blue) displays qualitatively a similar behaviour.

Figure 7 shows the size of NNLO corrections on $d\sigma/dt_{ee}$. In Setup 1, the correction along the electron line (red histogram) is slightly negative, never exceeding the -0.1% level, for $-0.12 \text{ GeV}^2 < t_{ee} < 0 \text{ GeV}^2$. For comparison, it is worth noticing that the NLO correction changes by about 10%, by looking at red line in the inset. For lower values (larger absolute values) of t_{ee} , the correction shows a steep increase to positive values, reaching about 1.5% at the kinematical boundary, where the NLO correction reaches about -18% w.r.t. the tree-level prediction. The NNLO correction along the muon line (blue histogram) displays a similar behaviour, as a function of t_{ee} , but with much smaller size: it does not exceed the 10^{-4} level in the window $-0.12 \text{ GeV}^2 < t_{ee} < 0 \text{ GeV}^2$ and reaches the size of about $+0.04\%$ at the kinematical boundary. The right panel of Fig. 7 shows the NNLO corrections when the acoplanarity cut is added (Setup 2). The electron-line correction is positive and increasing with increasing $|t_{ee}|$, from about 0.5% up to 3.2% at the boundary. This can be expected since the corresponding NLO correction on the electron line ranges from about -10% to -25% , because of the increased importance of the IR logarithm in the presence of cuts that tend to suppress hard photon emission. Also the NNLO correction along the muon line (blue histogram) is enhanced in the right panel

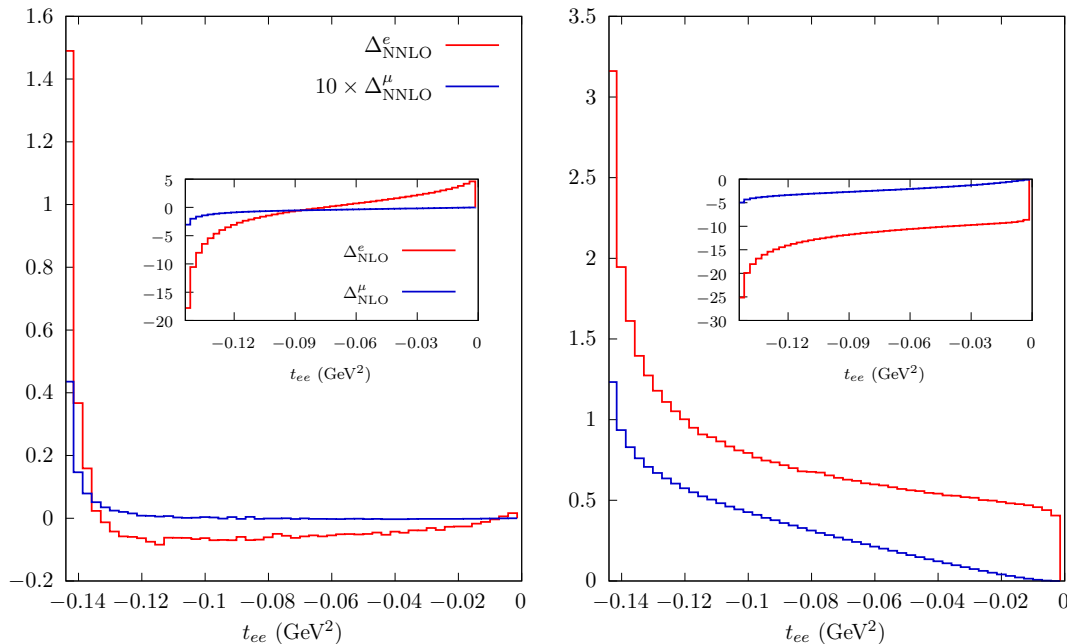


Figure 7. The same as Fig. 3 for the squared momentum transfer measured along the electron line, t_{ee} .

ranging from about 0% up to 0.13%. Correspondingly, the NLO correction shown in the inset ranges from 0% to -5%.

Finally, in Fig. 8 we consider the size of NNLO corrections on $d\sigma/dt_{\mu\mu}$. The behaviour of the corrections, as functions of $t_{\mu\mu}$, is similar to those of Fig. 7. In particular, for Setup 1, the correction along the electron (muon) line ranges from about 0% to 1% (0.04%) at the kinematical boundary. Also in the presence of the acoplanarity cut of Setup 2 (right panel), the shapes of the corrections are similar to the ones of Fig. 7, ranging from about 0.5% (0%) to 3% (0.13%) along the electron (muon) line.

4.2 Approximation to the full NNLO corrections

In Fig. 9, to be compared to Fig. 3, we show how the full (approximate) NNLO correction impacts the ϑ_e distribution. In absence of the acoplanarity cut (Setup 1, left panel), we notice how the NNLO correction is similar to the one stemming only from the electron line, except that at the left corner of the distribution is a few % larger for the μ^+ initiated process and smaller of a similar amount when μ^- is in the initial state. A more dramatic change is visible in Setup 2, when the acoplanarity cut is applied. For the $\mu^+e^- \rightarrow \mu^+e^-$ case, the NNLO corrections are similar to the electron-line corrections above ~ 5 mrad, but grow to 6.5% as $\vartheta_e \rightarrow 0$ mrad. For the $\mu^-e^- \rightarrow \mu^-e^-$ case instead, also in the region $\vartheta_e < 5$ mrad the NNLO correction remains moderate at the 0.5% level and almost flat. We remark that an analogous difference between μ^+ and μ^- is present also at NLO (see the insets and Figs. 10 and 11 of Ref. [28]) and that NNLO corrections tend to reduce the NLO ones. The variation in the corrections for different charge of the muon can be ascribed to

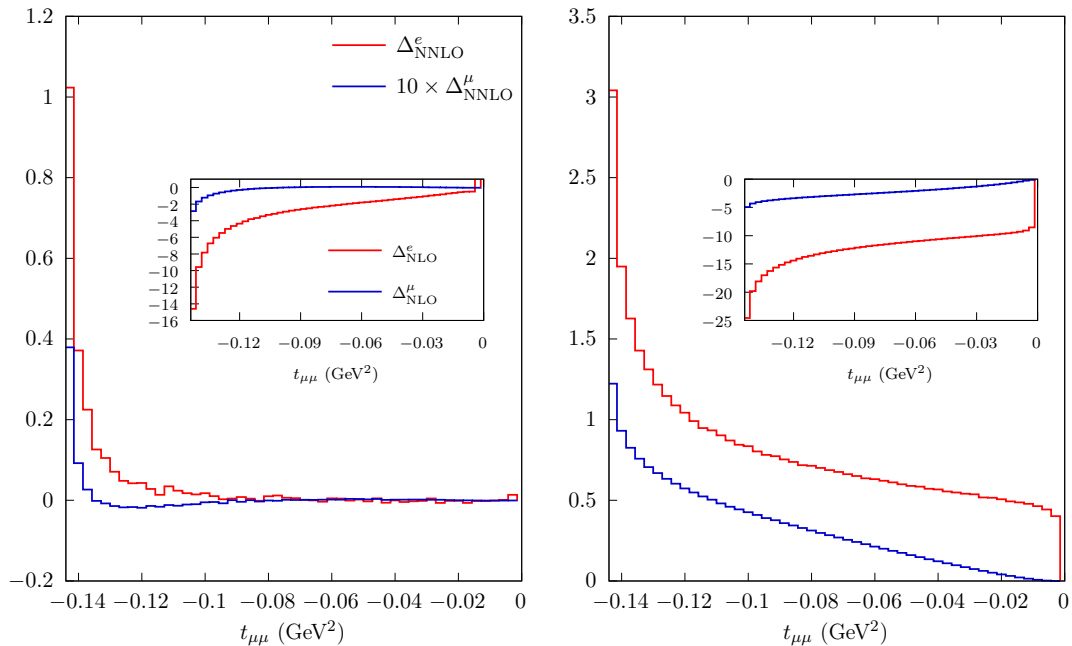


Figure 8. The same as Fig. 3 for the squared momentum transfer measured along the muon line, $t_{\mu\mu}$.

different radiation patterns, which interfere destructively in one case and constructively in the other one.

We finally show the NNLO effects on the t_{ee} distribution in Fig. 10, to be compared to Fig. 7. Also in this case, for Setup 1, the largest differences w.r.t. the corrections coming only from electron line occur for t_{ee} close to the kinematical limit $t_{ee}^{\min} \simeq -0.143 \text{ GeV}^2$, where the phase space allowed for radiation is restricted and IR effects are enhanced. For Setup 2, NNLO corrections are almost flat and of order 1% for incoming μ^- , while increase in size going from order 1% to 10% as t_{ee} goes from 0 GeV^2 to t_{ee}^{\min} for incoming μ^+ .

After discussing the numerical impact of the approximate full two-loop amplitude of Sect. 3 on relevant distributions, we conclude by examining its theoretical accuracy, which is necessarily an educated estimate since the exact calculation is not available yet. Firstly, we show how the one-loop box diagrams are approximated by their IR part as obtained from the YFS approach. In other terms, we compare the exact NLO virtual amplitude $\mathcal{M}^{\alpha 1}$ of Eq. (3.1) with the approximation

$$\widetilde{\mathcal{M}}^{\alpha 1} = \mathcal{M}_e^{\alpha 1} + \mathcal{M}_\mu^{\alpha 1} + Y_{e\mu} \mathcal{T}, \quad (4.4)$$

which can be thought as the NLO version of Eq. (3.6), or, otherwise, the latter can be seen as the NNLO generalization of the former. In Fig. 11, the difference of the exact NLO differential cross section and the approximate one, relative to LO, is shown as a function of the t_{ee} (left) and ϑ_e (right) variables. We remark that the difference ($d\sigma_{\text{NLO}}^{\text{approx}} - d\sigma_{\text{NLO}}$) depends on the charge of the incoming muon, as expected, but does not depend on the

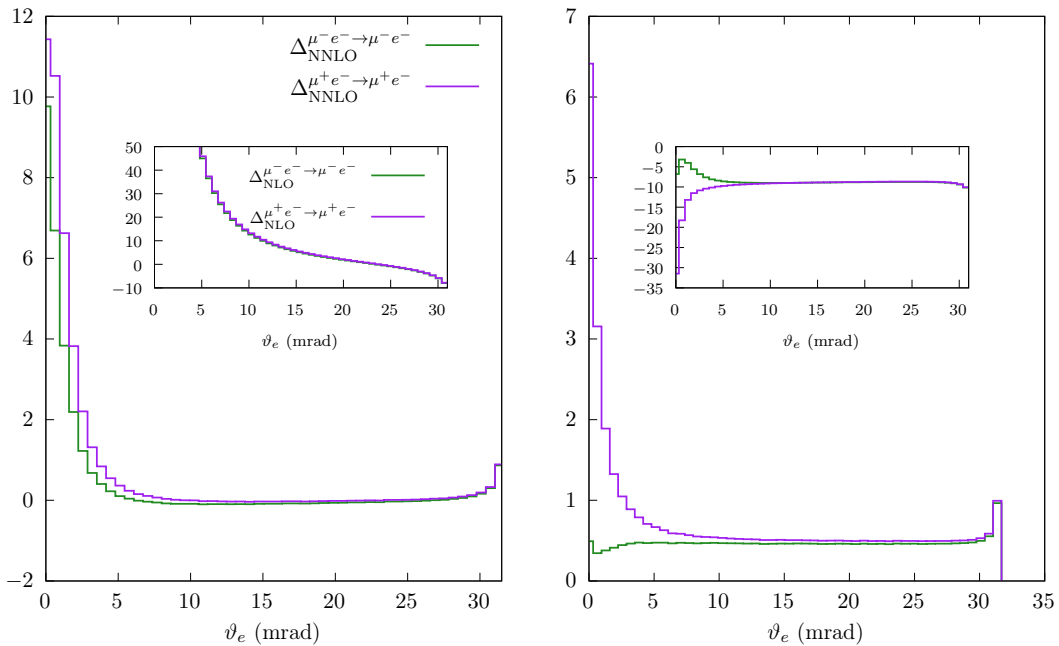


Figure 9. Approximation to the full NNLO corrections, according to Eq. (3.5) or (3.6), as a function of ϑ_e . The green histogram refers to the process $\mu^-e^- \rightarrow \mu^-e^-$ while the violet histogram refers to $\mu^+e^- \rightarrow \mu^+e^-$. Left panel: differential distribution in the presence of acceptance cuts only (Setup 1); right panel: the same as in the left panel with the additional acoplanarity cut of Setup 2. The insets report the NLO corrections, according to Eq. (4.3).

acoplanarity cut because only the virtual amplitude is modified. The approximation differs from the exact result at the level of 1-2%. We notice that this is of the same order of $\delta_{\text{NLO}} = \frac{\alpha}{\pi} \ln(m_\mu^2/m_e^2) \simeq 2.5\%$. This simple observation brings us to estimate the accuracy of Eq. (3.6) for the full two-loop amplitude to be of the order of $\delta_{\text{NLO}}^2 = \left(\frac{\alpha}{\pi}\right)^2 \ln^2(m_\mu^2/m_e^2) \simeq 6 \times 10^{-4}$.

Our estimate is further corroborated by noticing that the IR separation implied by Eq. (3.1) is not unique because non IR-terms can be freely moved from the Y factors to the $\mathcal{M}^{\alpha^{[1,2]},\text{R}}$ remnants. In our case, where we necessarily set $\mathcal{M}^{\alpha^2,\text{R}} = 0$ for diagrams with at least two photons connecting the e and μ lines, we can for instance switch off some non-IR terms in the second line of Eq. (3.6) to probe the size of the missing non-IR terms. For the sake of illustration, we accomplish this by setting to zero non-IR terms (which are also not singular in the limit of vanishing lepton masses) in the C_0 functions appearing in Eq. (3.3).

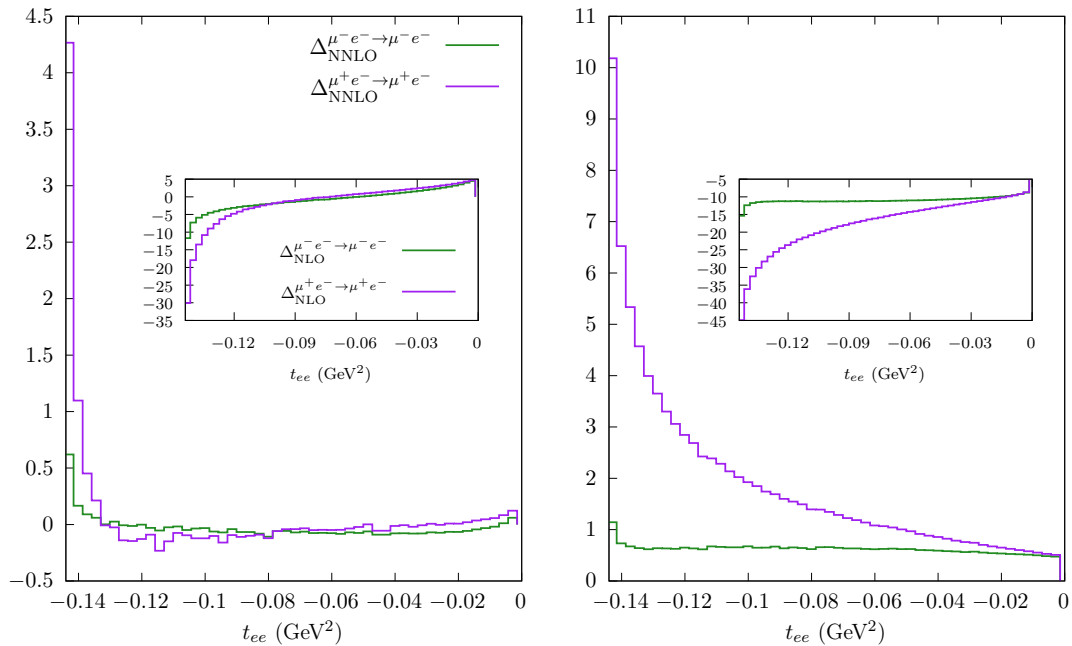


Figure 10. The same as Fig. 9 for the squared momentum transfer measured along the electron line, t_{ee} .

More explicitly, in the expression of the IR C_0 function (see Eq. (B.5) of Ref. [65])

$$\begin{aligned}
C_0 = \frac{x_s}{m_1 m_2 (1 - x_s^2)} & \left\{ -\ln\left(\frac{\lambda^2}{m_1 m_2}\right) \ln(x_s) - \frac{1}{2} \ln^2(x_s) + \frac{1}{2} \ln^2\left(\frac{m_1}{m_2}\right) \right. \\
& + 2 \ln(x_s) \ln(1 - x_s^2) - \frac{\pi^2}{6} + \text{Li}_2(x_s^2) \\
& \left. + \text{Li}_2\left(1 - x_s \frac{m_1}{m_2}\right) + \text{Li}_2\left(1 - x_s \frac{m_2}{m_1}\right) \right\}, \quad (4.5)
\end{aligned}$$

where $m_{1,2} = m_e$ or m_μ , λ is the vanishing photon mass and x_s is defined in Eq. (B.7) of Ref. [65], we remove the finite terms in second and third line of Eq. (4.5). We label this further NNLO approximation as $\overline{\text{YFS}}$ and in Fig. 12 we compare it to the standard one at differential level on the t_{ee} and ϑ_e distributions. The plots show that the (IR-safe) differences lie below the 2×10^{-4} range (in LO units), of the same size of the above estimate based on the NLO result.

5 Summary and prospects

In this work, we have analyzed the NNLO photonic corrections to $\mu^\pm e^- \rightarrow \mu^\pm e^-$ scattering and presented phenomenological results obtained with a related MC code, named MESMER. The study is motivated by the recent proposal of measuring the effective electromagnetic coupling constant in the space-like region by using this process (MUonE experiment). From the measurement of the hadronic contribution to the running of α_{QED} , the leading hadronic

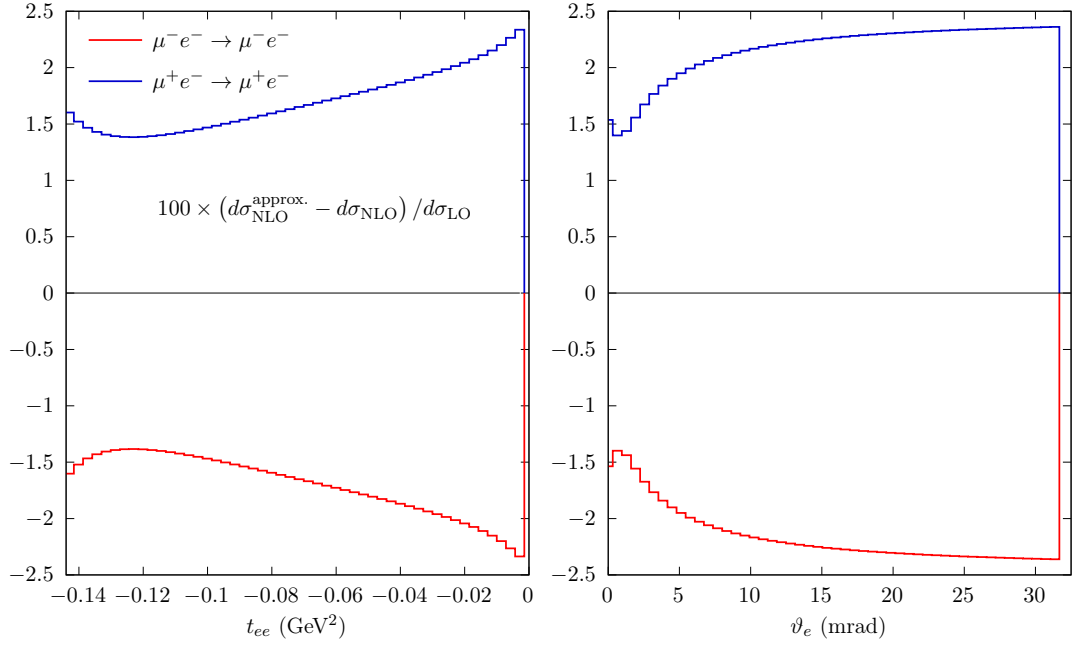


Figure 11. Difference between NLO box diagrams approximated *à la* YFS and the exact calculation, as a function of the t_{ee} (left) and ϑ_e (right) variables.

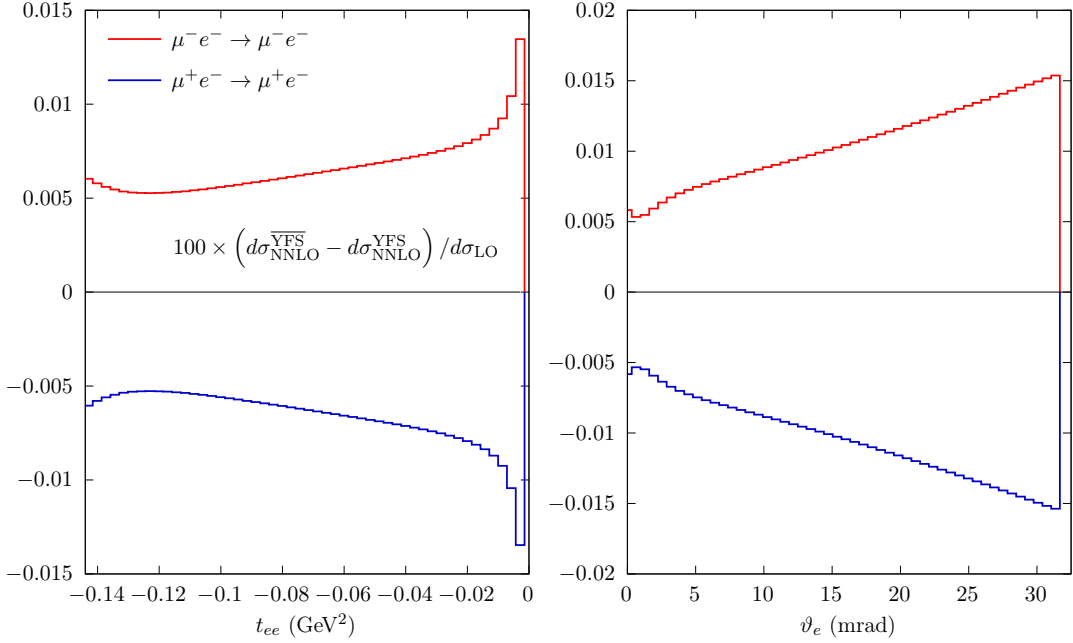


Figure 12. Difference between the alternative implementation of the YFS approximation described at the end of Sect. 4.2 and the standard one, as a function of the t_{ee} (left) and ϑ_e (right) variables.

contribution to the muon anomaly can be derived according to an alternative approach to the standard time-like evaluation of a_μ^{HLO} .

The calculation features the exact NNLO contribution of the gauge-invariant subset of QED photonic corrections along the leptonic legs, including all finite mass terms. The IR divergences are regularized by means of a small photon mass and a slicing photon energy parameter to separate soft from hard real radiation. The contribution of the vertex vacuum polarization insertion has been removed, in order to avoid potentially large logarithmic contributions which are cancelled by the real radiation of leptonic pairs, leaving the issue to a future investigation. The complete NNLO calculation, *i.e.* including also the up-down radiation contribution, has been calculated in an approximate way, since the complete NNLO virtual amplitudes are not yet available in the literature. Nevertheless, a YFS approach allows to approximate the missing NNLO virtual amplitudes with the correct inclusion of all IR enhanced terms. Moreover, the double-real radiation matrix elements as well as the phase space are exact, including all finite lepton mass effects. Also the NLO corrections to the $\mu^\pm e^- \rightarrow \mu^\pm e^- \gamma$ process, which are a part of the NNLO calculation, are exact.

The developed formalism has been implemented in a fixed-order generator able to reach NNLO accuracy for any differential cross sections. The structure of the code is completely general and the YFS approximation to the two-loop diagrams with at least two virtual photons connecting the electron and muon lines can easily be replaced with the corresponding exact amplitude, once available.

By means of the developed MC generator, we have extended a recent analysis from the NLO to the NNLO accuracy. In particular, we have considered a threshold electron energy of 1 GeV in the laboratory frame and two basic reference event selections: one involving only typical acceptance cuts of the MUonE experimental detector for the final state electron and muon; one including also a simplified acoplanarity cut to restrict the events around the elasticity curve given by the tree-level correlation between final state electron and muon scattering angles. We have considered a number of differential distributions, which allow to fully characterize the events of the MUonE experiment and to outline the best data analysis strategy to extract the HLO contribution to the running of the electromagnetic coupling constant in the space-like region.

The phenomenological study of the different observables points out that the size of the NNLO corrections, w.r.t. the LO differential cross-sections, is at the level of a few 10^{-4} for several regions of phase space in the presence of acceptance cuts only, leaving some corners of phase space where the corrections can grow up to the per cent level. As already remarked in the previous NLO analysis, the only exception is the electron scattering angle distribution which is particularly sensitive to photon radiation, in the region of small scattering angles where the LO prediction tends to zero as $\vartheta_e \rightarrow 0$. A similar feature of the LO prediction is also present for the muon scattering angle distribution, but in a very small range around $\vartheta_\mu \rightarrow 0$. Moreover, the typical size of the NNLO corrections grows up to the order of a few per mille in the presence of the acoplanarity cut, reaching the several per cent level at the boundaries of the phase space. This is a signal that IR terms start to dominate over the rest of the matrix elements (as already noticed in the NLO analysis) and definitely points

to the relevance of the next step of matching the fixed order calculation with an all order exclusive resummation procedure of multi-photon emission, for instance by generalizing to NNLO accuracy the matching of NLO corrections with a QED Parton Shower of Ref. [66]. This step is left to future work and it is by now under consideration.

Acknowledgments

We are sincerely grateful to all our MUonE colleagues for stimulating collaboration and many useful discussions, which are the framework of the present study. In particular we thank the PSI/Zurich group (P. Banerjee, T. Engel, A. Signer and Y. Ulrich) for continuous exchange and careful cross-check of our results, which helped to validate the technical precision of the developed Monte Carlo program. We are also indebted to P. Mastrolia and A. Primo for providing us with updated expressions of the two-loop form factors. The work of M.C. has been supported by the “Investissements d’avenir, Labex ENIGMASS”.

References

- [1] **Muon g-2** Collaboration, G. W. Bennett *et al.*, *Final Report of the Muon E821 Anomalous Magnetic Moment Measurement at BNL*, *Phys. Rev.* **D73** (2006) 072003, [[hep-ex/0602035](#)].
- [2] F. Jegerlehner and A. Nyffeler, *The Muon g-2*, *Phys. Rept.* **477** (2009) 1–110, [[0902.3360](#)].
- [3] F. Jegerlehner, *The Anomalous Magnetic Moment of the Muon*, *Springer Tracts Mod. Phys.* **274** (2017) pp. 1–693.
- [4] T. Aoyama *et al.*, *The anomalous magnetic moment of the muon in the Standard Model*, [2006.04822](#).
- [5] **Muon g-2** Collaboration, J. Grange *et al.*, *Muon (g-2) Technical Design Report*, [1501.06858](#).
- [6] **Fermilab E989** Collaboration, G. Venanzoni, *The New Muon g-2 experiment at Fermilab*, *Nucl. Part. Phys. Proc.* **273-275** (2016) 584–588, [[1411.2555](#)].
- [7] **J-PARC muon g-2/EDM** Collaboration, H. Iinuma, *New approach to the muon g-2 and EDM experiment at J-PARC*, *J. Phys. Conf. Ser.* **295** (2011) 012032.
- [8] **J-PARC g-2** Collaboration, T. Mibe, *Measurement of muon g-2 and EDM with an ultra-cold muon beam at J-PARC*, *Nucl. Phys. Proc. Suppl.* **218** (2011) 242–246.
- [9] F. Jegerlehner, *The Muon g-2 in Progress*, *Acta Phys. Polon.* **B49** (2018) 1157, [[1804.07409](#)].
- [10] A. Keshavarzi, D. Nomura, and T. Teubner, *The muon g – 2 and $\alpha(M_Z^2)$: a new data-based analysis*, *Phys. Rev.* **D97** (2018), no. 11 114025, [[1802.02995](#)].
- [11] M. Davier, A. Hoecker, B. Malaescu, and Z. Zhang, *A new evaluation of the hadronic vacuum polarisation contributions to the muon anomalous magnetic moment and to $\alpha(m_Z^2)$* , *Eur. Phys. J. C* **80** (2020), no. 3 241, [[1908.00921](#)]. [Erratum: *Eur.Phys.J.C* 80, 410 (2020)].
- [12] M. Della Morte, A. Francis, V. Gülpers, G. Herdoiza, G. von Hippel, H. Horch, B. Jäger, H. B. Meyer, A. Nyffeler, and H. Wittig, *The hadronic vacuum polarization contribution to the muon g – 2 from lattice QCD*, *JHEP* **10** (2017) 020, [[1705.01775](#)].

- [13] **Budapest-Marseille-Wuppertal** Collaboration, S. Borsanyi *et al.*, *Hadronic vacuum polarization contribution to the anomalous magnetic moments of leptons from first principles*, *Phys. Rev. Lett.* **121** (2018), no. 2 022002, [[1711.04980](#)].
- [14] H. B. Meyer and H. Wittig, *Lattice QCD and the anomalous magnetic moment of the muon*, [1807.09370](#).
- [15] H. B. Meyer and H. Wittig, *Lattice QCD and the anomalous magnetic moment of the muon*, *Prog. Part. Nucl. Phys.* **104** (2019) 46–96, [[1807.09370](#)].
- [16] **RBC, UKQCD** Collaboration, T. Blum, P. A. Boyle, V. Gülpers, T. Izubuchi, L. Jin, C. Jung, A. Jüttner, C. Lehner, A. Portelli, and J. T. Tsang, *Calculation of the hadronic vacuum polarization contribution to the muon anomalous magnetic moment*, *Phys. Rev. Lett.* **121** (2018), no. 2 022003, [[1801.07224](#)].
- [17] D. Giusti, F. Sanfilippo, and S. Simula, *Light-quark contribution to the leading hadronic vacuum polarization term of the muon $g - 2$ from twisted-mass fermions*, *Phys. Rev. D* **98** (2018), no. 11 114504, [[1808.00887](#)].
- [18] D. Giusti and S. Simula, *Ratios of the hadronic contributions to the lepton $g - 2$ from Lattice QCD+QED simulations*, [2003.12086](#).
- [19] S. Borsanyi *et al.*, *Leading-order hadronic vacuum polarization contribution to the muon magnetic moment from lattice QCD*, [2002.12347](#).
- [20] M. Dalla Brida, L. Giusti, T. Harris, and M. Pepe, *Multi-level Monte Carlo computation of the hadronic vacuum polarization contribution to $(g_\mu - 2)$* , [2007.02973](#).
- [21] B. Lautrup and E. de Rafael, *On sixth-order radiative corrections to the muon g -Factor*, *Nuovo Cim. A* **64** (1969) 322–324.
- [22] B. Lautrup, A. Peterman, and E. de Rafael, *Recent developments in the comparison between theory and experiments in quantum electrodynamics*, *Phys. Rept.* **3** (1972) 193–260.
- [23] C. M. Carloni Calame, M. Passera, L. Trentadue, and G. Venanzoni, *A new approach to evaluate the leading hadronic corrections to the muon g -2*, *Phys. Lett.* **B746** (2015) 325–329, [[1504.02228](#)].
- [24] G. Abbiendi *et al.*, *Measuring the leading hadronic contribution to the muon g -2 via μe scattering*, *Eur. Phys. J.* **C77** (2017), no. 3 139, [[1609.08987](#)].
- [25] A. B. Arbuzov, D. Haidt, C. Matteuzzi, M. Paganoni, and L. Trentadue, *The Running of the electromagnetic coupling α in small angle Bhabha scattering*, *Eur. Phys. J.* **C34** (2004) 267–275, [[hep-ph/0402211](#)].
- [26] **OPAL** Collaboration, G. Abbiendi *et al.*, *Measurement of the running of the QED coupling in small-angle Bhabha scattering at LEP*, *Eur. Phys. J.* **C45** (2006) 1–21, [[hep-ex/0505072](#)].
- [27] **MUonE** Collaboration, G. Abbiendi *et al.*, *Letter of Intent: the MUonE project*, Tech. Rep. CERN-SPSC-2019-026, SPSC-I-252, CERN, Geneva, Jun, 2019.
- [28] M. Alacevich, C. M. Carloni Calame, M. Chiesa, G. Montagna, O. Nicrosini, and F. Piccinini, *Muon-electron scattering at NLO*, *JHEP* **02** (2019) 155, [[1811.06743](#)].
- [29] S. Di Vita, S. Laporta, P. Mastrolia, A. Primo, and U. Schubert, *Master integrals for the NNLO virtual corrections to μe scattering in QED: the non-planar graphs*, [1806.08241](#).
- [30] P. Mastrolia, M. Passera, A. Primo, and U. Schubert, *Master integrals for the NNLO virtual corrections to μe scattering in QED: the planar graphs*, *JHEP* **11** (2017) 198, [[1709.07435](#)].

- [31] T. Engel, C. Gnendiger, A. Signer, and Y. Ulrich, *Small-mass effects in heavy-to-light form factors*, *JHEP* **02** (2019) 118, [[1811.06461](#)].
- [32] T. Engel, A. Signer, and Y. Ulrich, *A subtraction scheme for massive QED*, *JHEP* **01** (2020) 085, [[1909.10244](#)].
- [33] M. Fael and M. Passera, *Muon-Electron Scattering at Next-To-Next-To-Leading Order: The Hadronic Corrections*, *Phys. Rev. Lett.* **122** (2019), no. 19 192001, [[1901.03106](#)].
- [34] M. Fael, *Hadronic corrections to μ -e scattering at NNLO with space-like data*, *JHEP* **02** (2019) 027, [[1808.08233](#)].
- [35] A. Masiero, P. Paradisi, and M. Passera, *New physics at the MUonE experiment at CERN*, [2002.05418](#).
- [36] P. B. Dev, W. Rodejohann, X.-J. Xu, and Y. Zhang, *MUonE sensitivity to new physics explanations of the muon anomalous magnetic moment*, *JHEP* **05** (2020) 053, [[2002.04822](#)].
- [37] P. Banerjee *et al.*, *Theory for muon-electron scattering @ 10ppm: A report of the MUonE theory initiative*, *Eur. Phys. J. C* **80** (2020), no. 6 591, [[2004.13663](#)].
- [38] D. R. Yennie, S. C. Frautschi, and H. Suura, *The infrared divergence phenomena and high-energy processes*, *Annals Phys.* **13** (1961) 379–452.
- [39] P. Banerjee, T. Engel, A. Signer, and Y. Ulrich, *QED at NNLO with MCMULE*, *SciPost Phys.* **9** (2020) 027, [[2007.01654](#)].
- [40] G. 't Hooft and M. J. G. Veltman, *Scalar One Loop Integrals*, *Nucl. Phys.* **B153** (1979) 365–401.
- [41] A. Denner, *Techniques for calculation of electroweak radiative corrections at the one loop level and results for W physics at LEP-200*, *Fortsch. Phys.* **41** (1993) 307–420, [[0709.1075](#)].
- [42] A. Denner and S. Dittmaier, *Electroweak Radiative Corrections for Collider Physics*, *Phys. Rept.* **864** (2020) 1–163, [[1912.06823](#)].
- [43] J. Kuipers, T. Ueda, J. A. M. Vermaseren, and J. Vollinga, *FORM version 4.0*, *Comput. Phys. Commun.* **184** (2013) 1453–1467, [[1203.6543](#)].
- [44] B. Ruijl, T. Ueda, and J. Vermaseren, *FORM version 4.2*, [1707.06453](#).
- [45] A. Denner, S. Dittmaier, and L. Hofer, *Collier: a fortran-based Complex One-Loop Library in Extended Regularizations*, *Comput. Phys. Commun.* **212** (2017) 220–238, [[1604.06792](#)].
- [46] T. Hahn, *Feynman Diagram Calculations with FeynArts, FormCalc, and LoopTools*, *PoS ACAT2010* (2010) 078, [[1006.2231](#)].
- [47] T. Hahn and M. Perez-Victoria, *Automatized one loop calculations in four-dimensions and D-dimensions*, *Comput. Phys. Commun.* **118** (1999) 153–165, [[hep-ph/9807565](#)].
- [48] W. Bernreuther, R. Bonciani, T. Gehrmann, R. Heinesch, T. Leineweber, P. Mastrolia, and E. Remiddi, *Two-loop QCD corrections to the heavy quark form-factors: The Vector contributions*, *Nucl. Phys.* **B706** (2005) 245–324, [[hep-ph/0406046](#)].
- [49] J. Gluza, A. Mitov, S. Moch, and T. Riemann, *The QCD form factor of heavy quarks at NNLO*, *JHEP* **07** (2009) 001, [[0905.1137](#)].
- [50] P. Mastrolia and E. Remiddi, *Two loop form-factors in QED*, *Nucl. Phys.* **B664** (2003) 341–356, [[hep-ph/0302162](#)].

- [51] F. A. Berends, W. L. van Neerven, and G. J. H. Burgers, *Higher Order Radiative Corrections at LEP Energies*, *Nucl. Phys.* **B297** (1988) 429. [Erratum: *Nucl. Phys.*B304,921(1988)].
- [52] G. J. H. Burgers, *On the Two Loop QED Vertex Correction in the High-energy Limit*, *Phys. Lett.* **164B** (1985) 167–169.
- [53] J. Ablinger, A. Behring, J. Blümlein, G. Falcioni, A. De Freitas, P. Marquard, N. Rana, and C. Schneider, *Heavy quark form factors at two loops*, *Phys. Rev. D* **97** (2018), no. 9 094022, [[1712.09889](#)].
- [54] J. Blümlein, P. Marquard, N. Rana, and C. Schneider, *The Heavy Fermion Contributions to the Massive Three Loop Form Factors*, *Nucl. Phys. B* **949** (2019) 114751, [[1908.00357](#)].
- [55] J. Ablinger, J. Blümlein, P. Marquard, N. Rana, and C. Schneider, *Automated Solution of First Order Factorizable Systems of Differential Equations in One Variable*, *Nucl. Phys. B* **939** (2019) 253–291, [[1810.12261](#)].
- [56] J. Blümlein, P. Marquard, and N. Rana, *Asymptotic behavior of the heavy quark form factors at higher order*, *Phys. Rev. D* **99** (2019), no. 1 016013, [[1810.08943](#)].
- [57] J. Ablinger, J. Blümlein, P. Marquard, N. Rana, and C. Schneider, *Heavy Quark Form Factors at Three Loops in the Planar Limit*, *Phys. Lett. B* **782** (2018) 528–532, [[1804.07313](#)].
- [58] G. Montagna, M. Moretti, O. Nicrosini, A. Pallavicini, and F. Piccinini, *Light pair correction to Bhabha scattering at small angle*, *Nucl. Phys.* **B547** (1999) 39–59, [[hep-ph/9811436](#)].
- [59] R. Bonciani, A. Ferroglia, P. Mastrolia, E. Remiddi, and J. J. van der Bij, *Two-loop $N(F)=1$ QED Bhabha scattering differential cross section*, *Nucl. Phys.* **B701** (2004) 121–179, [[hep-ph/0405275](#)].
- [60] S. Actis, A. Denner, L. Hofer, J.-N. Lang, A. Scharf, and S. Uccirati, *RECOLA: REcursive Computation of One-Loop Amplitudes*, *Comput. Phys. Commun.* **214** (2017) 140–173, [[1605.01090](#)].
- [61] S. Jadach, B. Ward, and Z. Was, *Coherent exclusive exponentiation for precision Monte Carlo calculations*, *Phys. Rev. D* **63** (2001) 113009, [[hep-ph/0006359](#)].
- [62] M. Schönherr and F. Krauss, *Soft Photon Radiation in Particle Decays in SHERPA*, *JHEP* **12** (2008) 018, [[0810.5071](#)].
- [63] F. Krauss, J. M. Lindert, R. Linten, and M. Schönherr, *Accurate simulation of W , Z and Higgs boson decays in Sherpa*, *Eur. Phys. J. C* **79** (2019), no. 2 143, [[1809.10650](#)].
- [64] R. Linten, *Precision simulations in Drell-Yan production processes*. PhD thesis, Durham U. (main), 2018.
- [65] S. Dittmaier, *Separation of soft and collinear singularities from one loop N point integrals*, *Nucl. Phys. B* **675** (2003) 447–466, [[hep-ph/0308246](#)].
- [66] G. Balossini, C. M. Carloni Calame, G. Montagna, O. Nicrosini, and F. Piccinini, *Matching perturbative and parton shower corrections to Bhabha process at flavour factories*, *Nucl. Phys.* **B758** (2006) 227–253, [[hep-ph/0607181](#)].